Spatiotemporal Koopman decomposition of second mode instability from a hypersonic schlieren video ⊘

Arman C. Ghannadian [ID] ; Ryan C. Gosse [ID] ; Subrata Roy [✉] [ID] ; Zachary D. Lawless [ID] ; Samantha A. Miller; Joseph S. Jewell [ID]

Check for updates

View Online   Export Citation

Physics of Fluids

Special Topic:
Recent Advances in Fluid Dynamics and its Applications

Guest Editors: B.Reddappa, B. Rushi Kumar, Sreedhara Rao Gunakala, Bijula Prabhakar Reddy

Submit Today!

AIP Publishing

Spatiotemporal Koopman decomposition of second mode instability from a hypersonic schlieren video

View Online   Export Citation   CrossMark

Arman C. Ghannadian,[1] (iD) Ryan C. Gosse,[1] (iD) Subrata Roy,[1,a] (iD) Zachary D. Lawless,[2] (iD) Samantha A. Miller,[2] and Joseph S. Jewell[2] (iD)

AFFILIATIONS

[1]Department of Mechanical and Aerospace Engineering, University of Florida, Gainesville, Florida 32611, USA
[2]School of Aeronautics and Astronautics, Purdue University, West Lafayette, Indiana 47907, USA

[a]Author to whom correspondence should be addressed: roy@ufl.edu

ABSTRACT

Data-driven modal analysis methods provide a powerful way to decompose data into a sum of modes. The spatiotemporal Koopman decomposition (STKD) enables the computation of modes defined by global frequencies and growth rates in various spatial dimensions and time. The method is an extension of the dynamic mode decomposition (DMD) and higher-order dynamic mode decomposition (HODMD) that represents the data as a sum of standing and traveling, possibly growing or decaying, waves. In this paper, the STKD with HODMD is applied to schlieren video highlighting second mode instability waves traveling down the length of a 3-degree half-angle cone and a 7-degree half-angle cone, both at a freestream Mach number of 6. The HODMD is able to compute dominant modes and frequencies that align with those from associated experimental measurements of unsteady pressure fluctuations, and whose mode shapes clearly show the intensifying wavepacket structure of the waves. The STKD algorithm is used to compute streamwise wavenumbers, spatial growth rates, and wave speeds. The spatial growth rates from the STKD and the magnitudes of the HODMD mode shapes are used to compute the N-factor for waves of several frequencies. Overall, the STKD with HODMD is shown to be a useful tool for extracting spatiotemporal disturbance growth from a schlieren video.

Published under an exclusive license by AIP Publishing. https://doi.org/10.1063/5.0226443

I. INTRODUCTION

Transition prediction is vital for hypersonic flight as the onset of turbulence can significantly impact important flight characteristics such as surface heating and drag. An understanding of hydrodynamic stability is necessary to gain insight into the complex process of transition. The fundamental work done by Mack[1] summarizing linear stability theory (LST) is well-known. Specifically, Mack's second mode is an instability mechanism that selectively amplifies high-frequency acoustic waves that remain within the sonic line in the boundary layer. For flow regimes at a Mach number greater than 4 over flat plates and cones at zero angle of attack, it is known that this second mode becomes the dominant instability mechanism as it is associated with the largest amplification rate.

Initially a solution to the LST equations, Mack's second mode instability is studied via more sophisticated analyses such as parabolized stability equations (PSE)[2] for more complex flows. Numerical simulations used for stability calculations can become exceedingly costly, however. Experimental measurements of instability mechanisms contain the true physics without limiting assumptions such as linearization of the flow. However, experiments, especially in the hypersonic regime, come with a wide range of difficulties. Pressure sensors can be used to measure pressure fluctuations which can be used to estimate modal frequencies, but identifying growths of disturbances like instability waves that evolve spatially with a given frequency can be more challenging. Thus, it is desirable to look at other sources of unsteady data like schlieren videography to extract this type of information.

In this paper, the effectiveness of a data-driven modal decomposition method, the spatiotemporal Koopman decomposition (STKD) developed by Le Clainche and Vega[3] (discussed below), is examined through computation of second mode instability growth from experimental schlieren video. The goal of implementing this algorithm is to show a fast and computationally inexpensive method of estimating second mode growth from experimental schlieren, a data source

primarily used for flow visualization. The implications of this purely data-driven method are wide-reaching, and the algorithm could be applied as a low-cost method for estimating growth of any signal in a flow-field from schlieren or other unsteady data sources. The novelty of this paper is the application of STKD to extract spatial growth rates of second mode waves from schlieren video along with associated wave speeds. To the authors' knowledge, this is the first application of STKD for a coupled spatiotemporal analysis of experimental measurements of second mode instability waves. However, separate temporal and spatial analyses have been done to compute the growth of instability waves. For example, authors applied dynamic mode decomposition (DMD)[4] and later higher-order DMD (HODMD)[5] for a purely spatial analysis to estimate the spatial growth of TS waves from numerical simulation data for flow over an airfoil.[6,7] Another study used HODMD spatial analysis to analyze cross-flow instabilities over an airfoil.[8] Additionally, other studies have used temporal analyses to examine spatial mode shapes and their associated time dynamics with various modal analysis techniques including DMD from schlieren.[9] Most previous studies have used modal analysis methods like DMD for spatial or temporal analyses of schlieren or of instabilities from computational or experimental data. The approaches in the present paper have the advantage of isolating spatial growth rates for waves with specific temporal frequencies, constituting a coupled spatiotemporal analysis of second mode instability waves from experimental schlieren.

Data-driven modal decomposition such as the proper orthogonal decomposition (POD)[10] and DMD have been used for a wide variety of physical problems and are commonly used in fluid dynamics to analyze complex or turbulent flow-fields.[11] The DMD algorithm, however, poorly represents data that have a higher spectral complexity than spatial complexity.[5] Here, spectral complexity is related to the number of frequencies and damping rates required to represent a dataset, while spatial complexity is the dimension of the vector space spanned by the DMD modes. Each DMD mode has only one frequency and one growth rate, so the number of frequencies that can be computed is limited by the spatial complexity. This is a fundamental limitation in the DMD algorithm, which computes eigenvectors of a best-fit matrix that advances snapshots one time step into the future. The rank of this best-fit matrix is then the spatial complexity of the data. The DMD makes the approximation for a snapshot matrix V of size $I \times K$ that

$$V_2^K \approx R V_1^{K-1}, \tag{1}$$

where R is the matrix whose eigenvectors give DMD modes. The superscript here denotes the last column being taken, and the subscript denotes the first. Thus, the right-hand side matrix V_1^{K-1} contains all but the last column of V. Then, this best-fit matrix R has only at most the rank of the set of snapshots and accordingly has a limited number of eigenvectors corresponding to non-zero eigenvalues. The rank is further limited by a dimension reduction with an initial truncated singular value decomposition (SVD) that is often used to filter out noise or small flow scales that could be undesirable. The issue of limited spatial complexity arises when data are either spatially undersampled (a time series from a single spatial point would have a rank of one, for example) or when an optimal rank truncation has been done via a truncated SVD-based method.

The HODMD overcomes the issue of spatial complexity by using time-lagged snapshots. The HODMD assumes there are d matrices

that relate $d + 1$ snapshots to each other, where d is the delay parameter. The higher-order Koopman assumption encapsulates this as

$$\mathbf{v}_{k+d} = R_1 \mathbf{v}_k + R_2 \mathbf{v}_{k+1} + \cdots + R_d \mathbf{v}_{k+d-1}, \tag{2}$$

for $k = 1, \ldots K - d$, where $\mathbf{v}_k$ are columns of the snapshot matrix. This ideally enlarges the dimension of the data for the spectral complexity of the data to be better captured. The problem of larger spectral complexity than spatial complexity is well-known for the standard DMD, as[12,29] emphasized the DMD cannot compute all oscillatory dynamics that exist in a subspace with a rank less than twice the number of expected frequencies. This is because two DMD modes are required to capture one frequency, a complex-conjugate pair. The exact algorithm will be summarized in more detail in Sec. II. The HODMD method is used here because many fluid dynamics problems have larger spectral complexity than spatial complexity, and experimental data like schlieren video have inherent noise that adds non-physical spectral complexity to a degree that can cause standard DMD to provide spurious results. As will be discussed in this paper, standard DMD produced good results for the purely temporal decomposition. However, a mix of standard DMD and HODMD was required for the spatiotemporal analysis.

In addition to the benefits above, the HODMD method has been shown to converge to finding peak frequencies faster than other modal decomposition techniques including standard DMD, POD, and spectral POD (SPOD)[13] from limited data for several different fluid dynamics simulations.[14] Both HODMD and standard DMD methods result in modes $\mathbf{u}$ that are functions of space only and modulated by sinusoids that can grow or decay exponentially. This is represented in Eq. (3) as

$$v(\xi_i, t_k) \approx \sum_{n=1}^{N} a_n u_n(\xi_i) e^{(\delta_n + i\omega_n)t_k}, \tag{3}$$

where the spatial indices have been collected and stacked so that each snapshot, and therefore each mode, is a vector of length equal to the number of spatial points. Thus, ξ parametrizes points along all the spatial dimensions of the dataset organized consistently into entries of a single vector. The data can be organized as a higher-order tensor as well. However, this changes the algorithm slightly as discussed below, and it requires the application of a higher-order singular value decomposition (HOSVD). Using the HOSVD allows for better noise removal in many cases than the standard truncated SVD, as will be discussed in subsequent sections.[26,28]

The HOSVD is necessary for the multidimensional extension of HODMD that Le Clainche and Vega first developed to obtain modes with explicit spatial and temporal growth rates, frequencies, and spatial wavenumbers, the STKD.[3] The STKD allows for expansions of the form

$$v(x_i, y_j, t_k) \approx \sum_{m=1}^{M} \sum_{n=1}^{N} a_{mn} u_{mn}(y_j) e^{(\nu_m + i\kappa_m)x_i + (\delta_n + i\omega_n)t_k}, \tag{4}$$

where the modes u could be functions of a spatial coordinate or not, and as many spatial coordinates could be included in the exponential as is desired. Generally, the benefits of enhanced filtering through the HOSVD and the robustness of the HODMD method lend the STKD to be more well suited for complex multiscale or turbulent flows than

traditional DMD methods. The STKD has been applied to analyze vortices in urban environments,[15] flows around offshore wind turbines,[16] a zero-net-mass-flux jet,[17] and a 3D cylinder wake.[18] For the analysis in this paper, x is taken to be the surface-tangent coordinate along the streamwise direction of the cone, and the expression of interest is exactly that defined in Eq. (4).

The outline of the rest of this paper is as follows. First, the algorithms for HODMD and then STKD are presented. This is because there are many DMD-like methods and variations of the algorithms, so it is important to outline the steps taken in the present study. Then, the experimental setup is described along with a note about the application of the methods to schlieren video. The Boeing/AFOSR Mach 6 Quiet Tunnel (BAM6QT) was used for the schlieren videography because of its unique quiet run capability, allowing for the second mode waves to be seen more clearly. Next, results for standard DMD (equivalent to HODMD with a delay parameter of one) are presented. An estimation of noise levels based on DMD-1 is given. This is then used to choose the truncation tolerance for HODMD with a delay parameter greater than one. Finally, the HODMD and STKD analyses are presented. These methods are shown to be useful for extracting important flow features such as modal frequencies, wavenumbers, spatial growth rates, and wave speeds from the schlieren video. The process described in this study suggests that application of STKD to schlieren video can give fast, low-cost estimates of growth rates of second mode instability waves in the flow in addition to the other parameters mentioned above. This is an improvement over traditional computationally costly numerical simulations which make limiting assumptions such as small-amplitude perturbations or linearization of the flow and other experimental measurements where it can be difficult to obtain a full picture of the flow phenomenon being analyzed. In addition, the usefulness of the STKD is not limited to instability waves as has been discussed in the papers mentioned above. Therefore, implications of applying the STKD to schlieren videos can be extended to extract the dynamics of many flow features from schlieren video where spatially evolving structures are involved.

II. HODMD ALGORITHM

The HODMD algorithm, also termed the DMD-d algorithm, is summarized here for completeness. For a detailed derivation of the method and its properties, see the original paper by Le Clainche and Vega.[5] The first step is to start with the truncated (to rank r) economy-size SVD of the snapshot matrix of size $I \times K$, written as

$$V = X\Sigma T^T. \tag{5}$$

Here, X is of size $I \times r$, Σ is $r \times r$, and T is $K \times r$. The truncation parameter is determined based on the magnitudes of the singular values σ. Namely, r is chosen so that the relative root mean square error (RRMSE) of the SVD reconstruction is

$$\text{RRMSE} = \sqrt{\frac{\sigma_{r+1} + \sigma_{r+2} + \cdots + \sigma_{\text{final}}}{\sigma_1 + \sigma_2 + \cdots + \sigma_{\text{final}}}} \leq \varepsilon_{svd,1}. \tag{6}$$

The RRMSE is defined as

$$\text{RRMSE} \equiv \frac{||V - V_{\text{DMD}}||_F}{||V||_F}. \tag{7}$$

Alternatively, the tolerance could be implemented so that

$$\frac{\sigma_{r+1}}{\sigma_1} \leq \varepsilon_{SVD,1}. \tag{8}$$

A dimension reduction could also be obtained via a truncated higher-order singular value decomposition (HOSVD) which represents the data as

$$V_{ijk} \approx \sum_{p_3=1}^{P_3} \sum_{p_2=1}^{P_2} \sum_{p_1=1}^{P_1} S_{p_1 p_2 p_3} X_{ip_1} Y_{jp_2} T_{kp_3}. \tag{9}$$

The data must initially be organized as a snapshot tensor for the HOSVD, $V_{ijk} = V(x_i, y_j, t_k)$. The HOSVD allows for better noise removal by allowing for SVD truncations in each dimension of the tensor. This gives singular values corresponding to each dimension as well (σ^x, σ^y, σ^t). The tolerance $\varepsilon_{\text{HOSVD}}$ can be different along each dimension. The temporal modes T are then rescaled as

$$\hat{T} = \Sigma T^T \tag{10}$$

if a standard truncated SVD was performed or as

$$\hat{T}_{p_3 k} = \sigma^t_{p_3} T_{p_3 k} \tag{11}$$

if an HOSVD was used initially. The columns of $\hat{T}$, denoted $\hat{\mathbf{t}}$, are referred to as the reduced snapshots. The higher-order Koopman assumption is applied to the reduced snapshots as

$$\hat{T}^K_{d+1} \approx \hat{R}_1 \hat{T}^{K-d}_1 + \hat{R}_2 \hat{T}^{K-d+1}_2 + \cdots + \hat{R}_d T^{K-1}_d. \tag{12}$$

The algorithm proceeds by reshaping this equation into one containing modified snapshots as

$$\tilde{T}^{K-d+1}_2 \approx \tilde{R}\tilde{T}^{K-d}_1, \tag{13}$$

where the columns $\tilde{\mathbf{t}}_k$ are

$$\tilde{\mathbf{t}}_k = \begin{bmatrix} \hat{\mathbf{t}}_k \\ \hat{\mathbf{t}}_{k+1} \\ \cdots \\ \hat{\mathbf{t}}_{k+d-1} \end{bmatrix}. \tag{14}$$

A final truncated SVD is then applied to filter out any redundancies resulting from this process, which gives the equation for the reduced modified snapshots as

$$\bar{T}^{K-d+1}_2 \approx \bar{R}\bar{T}^{K-d}_1. \tag{15}$$

A second tolerance $\varepsilon_{svd,2}$ is used for this truncation. The reduced modified snapshots $\bar{T}$ above are given as the product of the singular value matrix and the transpose of the matrix of right singular vectors from the truncated SVD of $\tilde{T}$, just as the reduced snapshots are computed from the SVD matrices of the snapshot matrix. The matrix $\bar{R}$ is solved for with a pseudo-inverse. The eigenvalues of the $\bar{R}$, λ_n, give the growth rates and frequencies based on the relation

$$\delta_n + i\omega_n = \frac{\ln(\lambda_n)}{\Delta t}. \tag{16}$$

The eigenvectors of $\bar{R}$ give those of $\tilde{R}$ when left-multiplied by the matrix of left singular vectors of $\tilde{T}$ (obtained through the final truncated SVD mentioned above). The first P_3 (or r) components of each

of the eigenvectors of $\tilde{R}$ are the reduced modes $\hat{\mathbf{u}}$. The expansion now reads

$$\hat{\mathbf{t}} \approx \sum_{n=1}^{N} a_n \hat{\mathbf{u}}_n e^{(\delta_n + i\omega_n)t_k}. \tag{17}$$

The reduced modes $\hat{\mathbf{u}}_n$ are rescaled to have unit RMS Frobenius norm. Then, the amplitudes are solved for via a least squares fit of the above expansion to the reduced snapshots $\hat{\mathbf{t}}$. They are then truncated based on the tolerance ε_{amp} such that only modes with

$$\frac{a_n}{a_{\max}} \geq \varepsilon_{amp} \tag{18}$$

are kept. Then, the final HODMD modes for the standard SVD version of the method are found by left-multiplying the reduced modes by the matrix of left singular vectors of the reduced snapshots as

$$\mathbf{u}_n = X\hat{\mathbf{u}}_n. \tag{19}$$

For the HOSVD variant, the modes must be computed from the HOSVD modes as

$$u_{ijn} = \sum_{p_3=1}^{P_3} \sum_{p_2=1}^{P_2} \sum_{p_1=1}^{P_1} \frac{1}{\sigma_{p_3}^t} S_{p_1 p_2 p_3} X_{ip_1} Y_{jp_2} \hat{u}_{np_3}. \tag{20}$$

III. TWO-DIMENSIONAL STKD ALGORITHM

The STKD algorithm is summarized below for completeness, and Le Clainche and Vega give a complete description and derivation of the method in the original paper.[3] The first step is computing the HOSVD of the snapshot tensor. For clarity, the truncated HOSVD is written again here as the sum

$$V_{ijk} \approx \sum_{p_3=1}^{P_3} \sum_{p_2=1}^{P_2} \sum_{p_1=1}^{P_1} S_{p_1 p_2 p_3} X_{ip_1} Y_{jp_2} T_{kp_3}. \tag{21}$$

The HOSVD mode matrices are then rescaled by their singular values as

$$\hat{X}_{pi} = \sigma_{p_1}^x X_{p_1 i} \tag{22}$$

and

$$\hat{T}_{pk} = \sigma_{p_3}^t T_{p_3 k}. \tag{23}$$

The HODMD algorithm, excluding the initial truncated SVD, can then be applied to $\hat{X}$ and $\hat{T}$, which yields

$$\hat{T}_{p_3 k} \approx \sum_{n=1}^{N} a_n^t \hat{u}_{p_3 n}^t e^{(\delta_n + i\omega_n)t_k} \tag{24}$$

and

$$\hat{X}_{p_1 i} \approx \sum_{m=1}^{M} a_m^x \hat{u}_{p_1 m}^x e^{(\nu_m + i\kappa_m)x_i}. \tag{25}$$

Now, the non-normalized STKD modes are computed as

$$\tilde{u}_{mnj} = a_m^x a_n^t \sum_{p_3=1}^{P_3} \sum_{p_1=1}^{P_1} \hat{S}_{p_1 jp_3} \hat{u}_{p_1 m}^x \hat{u}_{p_3 n}^t, \tag{26}$$

where

$$\hat{S}_{p_1 jp_3} = \frac{1}{\sigma_{p_1}^x \sigma_{p_3}^t} \sum_{p_2=1}^{P_2} S_{p_1 p_2 p_3} Y_{jp_2}. \tag{27}$$

The STKD mode amplitudes are solved for as

$$a_{mn} = \frac{1}{\sqrt{J}} \sqrt{\sum_{j=1}^{J} [\tilde{u}_{mnj}]^2}, \tag{28}$$

for $a_{mn} > 0$. The STKD modes are then given as

$$u_{mnj} = \frac{\tilde{u}_{mnj}}{a_{mn}}. \tag{29}$$

Note that the above non-zero amplitudes are real and positive, and the modes exhibit unit RMS norm. With these definitions, the expressions (24)–(29) yield the desired expansion (4). Like the HODMD algorithm, the final amplitudes may be truncated so that only

$$\frac{a_{mn}}{\max(a_{mn})} \geq \varepsilon_{amp} \tag{30}$$

are kept. This value of ε_{amp} may or may not coincide with that used in the HODMD analysis of $\hat{X}$ and $\hat{T}$.

IV. EXPERIMENTAL SETUP

The Boeing/AFOSR Mach 6 Quiet Tunnel (BAM6QT) is a Ludwieg tube design engineered to achieve Mach 6 flow. The driver tube up to burst diaphragm section is pressurized to the desired stagnation pressure. The dual diaphragm configuration acts as a barrier between the vacuum tank and the pressurized tunnel segments. The tunnel is started by bursting both diaphragms, followed by the passage of an expansion fan through the throat, initiating Mach 6 flow within the test section.

This wind tunnel produces Mach 6 flow while maintaining an approximate free-stream noise level of 0.02%.[19] Quiet flow is achieved through a combination of a highly polished nozzle, long diverging sections, and boundary layer suction via bleed-slots at the nozzle throat. Disabling the bleed-slot suction during operation transitions the tunnel to a conventional mode, resulting in a free-stream noise level of approximately 3%.[19] The BAM6QT typically sustains operation for 4–5 s, with approximately 3 s of continuous quiet flow.[20,21]

A. 3-degree cone

The 3-degree cone model consists of a sharp 3-degree half-angle cone with a base diameter of 11.43 cm. The model is sting mounted. The cone is adjusted to have a 0 degree angle of attack. A simple model schematic can be seen in Fig. 1.

B. 7-degree cone

The 7-degree cone model consists of a sharp 7-degree half-angle cone with a 4.31 in. base. The strut is 0.43 in. thick and is mounted to the top of the tunnel. When mounted in the tunnel, the cone is assumed to be at a 0 degree angle of attack. A simple model schematic can be seen in Fig. 2.

V. APPLICATION OF HODMD AND STKD TO SCHLIEREN VIDEO

The frames of the schlieren video are matrices of gray-scale pixel values. For the HODMD with standard SVD, each frame, or snapshot, is reshaped into a column vector, and these column vectors are stacked sequentially into the snapshot matrix. Each column then contains all of the pixel values from the respective frame of the video, and each column represents the video one Δt from the previous. For the STKD and HODMD with HOSVD, the video is initially organized as a higher dimensional tensor where each index corresponds to a different dimension as in Eq. (4). In the present analysis, both videos are cropped to regions of interest, and 500 frames are taken. For the HODMD analysis, the desire was to obtain time dynamics associated with spatial modes $u(x, y)$. The spatial growth rates and wavenumbers are given implicitly by the mode shapes given by the temporal HODMD analysis. Thus, the STKD can be thought of as further decomposing the spatial information of each HODMD mode as a sum of potentially growing or decaying sinusoids in space and time to give explicit spatial dynamics as well.

The cropped regions of interest are shown for the videos in Figs. 3 and 4. These images contain the first frames of the unprocessed videos. For the 3-degree case, the image is flipped horizontally to show flow going left to right. In addition, the results shown hereafter assume the positive x-direction to be the streamwise direction. The video is confined to last approximately 9 cm of the length of the cone, and the video is oriented such that the camera is aligned with the cone surface.

Like the 3-degree cone video, the original unprocessed video of the 7-degree cone is flipped so that the flow moves left to right, and this is flipped for the rest of the analyses as well. The video shows the base corner of the cone and part of the base flow region. Additionally, the video is aligned with the freestream direction, so the base corner of the cone is seen pointing down with the cone surface tilted 7 degrees from the orientation of the video frame. Note that the colormap for the schlieren frames was adjusted uniformly from traditional grayscale for enhanced visibility.

VI. RESULTS AND DISCUSSION

A. DMD and HODMD

1. DMD-1 with standard SVD and no dimension reduction

For all cases analyzed here, DMD-1 has been applied to the mean-subtracted dataset with no SVD truncation ($\varepsilon_{SVD} \ll 1$). No truncation means the rank of the snapshots was not reduced. For the 3-degree cone case, the rank of the snapshot matrix was 499, so 499 SVD modes were kept. This was done because mean subtraction has been shown to improve results of SVD-based DMD.[22] This resulted in a very small reconstruction error compared to the mean-subtracted dataset, $RRMSE \approx 6.50 \times 10^{-13}$. The video has background noise, which can be seen in the DMD modes below, but the main features are highlighted clearly enough due to the high signal-to-noise ratio (SNR). The high SNR combined with the high spatial resolution of the video allowing for high spatial complexity to fully capture the spectral complexity of the data (when no truncation has been done to reduce the spatial complexity in an effort to remove noise) explains the good performance of the DMD-1 method for the cases presented here. Figure 5 shows the DMD-1 spectrum, where the eigenvalues are colored by their normalized amplitudes, as well as a plot of normalized amplitude vs frequencies and growth rates.

The plot of frequencies shows peaks around 101.50 and 106.75 kHz. In addition, higher harmonics of this frequency range are seen. This harmonic energy transfer is a known experimental phenomenon, and the peak frequencies here align closely with those from the corresponding pressure sensor data.[23] The closeness of computed frequencies to experimental PSD is expected too, as[24] showed an equivalence between the DMD and the discrete Fourier transform (DFT) when the mean is subtracted. However, Hirsh *et al.*[22] showed that this is only the case whenever the mean-subtracted dataset has full effective rank. Although the physics involved may be lower-rank, background noise causes the experimental dataset to be full rank. Thus, the similarity between the DMD and DFT persists—the growth rates are all approximately zero, which means that this dataset has been decomposed into a sum of non-decaying Fourier modes. The frequencies computed were all separated by $\Delta f = f_s/K$. This is exactly the output of a DFT applied to a signal. The reduction of DMD to a DFT is generally not desirable, as exponential growth in the signal will not be captured explicitly (only as the sum of a large number of purely oscillatory Fourier modes since the Fourier transform of a decaying exponential is a continuous function of frequency). However, for the time dynamics of the present datasets, finding exponential growth was not the goal, so frequencies close to experimental values along with spatial mode shapes that displayed the proper physics were considered adequate. However, as will be discussed later, this was not sufficient for the spatial analysis which sought to exploit exponential growth in space.

The DMD mode contours for the 106.75 kHz mode are shown in Fig. 6. The mode shapes clearly show the wavepacket structure of the
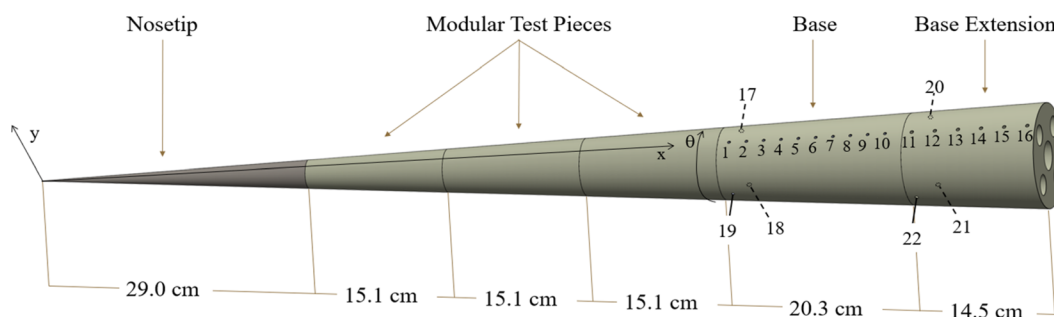

FIG. 1. Model schematic showing basic geometric details for 3-degree cone. All units are in inches unless otherwise noted.
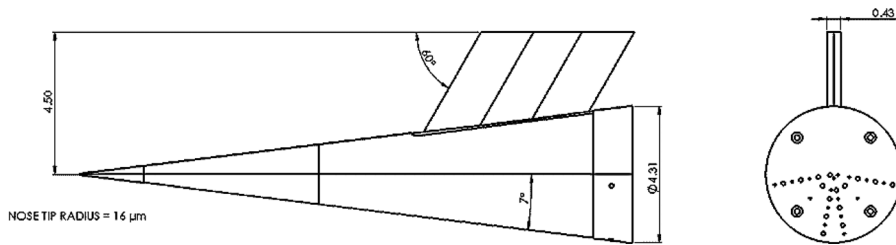
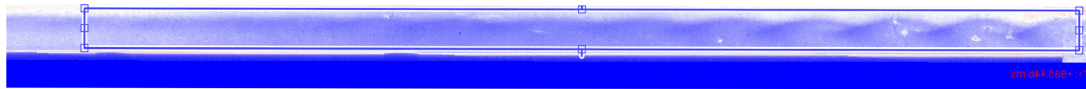**FIG. 2.** Model schematic showing basic geometric details for 7-degree cone. All units are in inches unless otherwise noted.

FIG. 3. Cropped region of interest for 3-degree cone. The image has been flipped horizontally so that flow goes left to right.
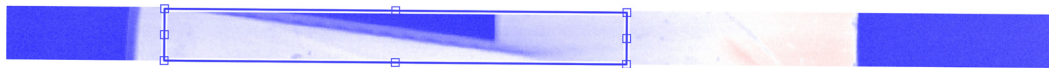

FIG. 4. Cropped region of interest for 7-degree cone. The image has been flipped to show the flow moving left to right.

second mode instability waves. The intensification of the signal as the wave travels downstream is shown in both the real and imaginary components. This is also made clear in the magnitude plot in Fig. 6(c), while the phase plot [Fig. 6(d)] more clearly shows the traveling nature of the disturbance. The relationship between amplitude and phase and the real and imaginary mode shapes is clarified by reconstructing the data based on one mode pair. This is due to the fact that complex modes computed from real-valued data with both nonzero imaginary parts and nonzero real parts come in complex-conjugate pairs. Letting an overbar denote the complex conjugate and the positive-frequency mode be $u(x,y) = \alpha(x,y) + i\beta(x,y)$, then $u(x,y)e^{i\omega t} + \bar{u}(x,y)e^{-i\omega t} = 2\alpha(x,y)\cos(\omega t) - 2\beta(x,y)\sin(\omega t)$. Then, the reconstruction based on a single mode pair, ignoring amplitude, can be written as

$$V_{\text{reconst}} = A(x,y)\cos[\omega t + \phi(x,y)], \qquad (31)$$

where the phase angle $\phi(x,y) = \operatorname{atan}^2[\beta(x,y), \alpha(x,y)]$, and $A(x,y)$ is twice the magnitude of the single DMD mode. Note that $A(x,y)$ is different than the amplitude associated with each mode—each mode is scaled to have unit RMS Frobenius norm and $A(x,y)$ is the variation in the value of the mode shape. A small distinction that must be noted, however, is that when looking at a single DMD mode the phase may have a flipped sign. This is because the negative-frequency mode in the complex-conjugate pair will have a phase of $\phi(x,y) = \operatorname{atan}^2[-\beta(x,y), \alpha(x,y)]$. The positive frequency mode will have a phase that matches the sum of the contribution of the two modes.

For the 7-degree cone, a similarly low reconstruction error was seen when applying DMD-1 to the mean-subtracted schlieren video. The reconstruction error was $RRMSE \approx 6.45 \times 10^{-13}$. The DMD-1 spectrum along with the frequencies and growth rates is given in Fig. 7. Again, there is a high-frequency mode that represents incoherent noise at 473.5 kHz, half the sampling frequency. The peak frequencies are clearly identifiable in Fig. 7(b). The peak frequencies corresponding to the second mode waves were around 275 kHz. The highest amplitude DMD-1 mode corresponding to the second mode

instability waves had a frequency of 278.25 kHz. There are several other high-amplitude modes close to this frequency as well.

The contours of the third DMD-1 mode corresponding to a peak frequency of 278.25 kHz are given in Fig. 8. The peak frequencies here align closely with STABL PSE computations. The real and imaginary parts visualize the wavepacket structure, while the magnitude and phase show the increasing wave intensity and traveling nature, respectively. These mode shapes align with the published SPOD results for the schlieren video.[25] The instability waves are shown to follow the expansion around the base corner and showed that the peak second mode frequencies were found in the power spectrum of unsteady base pressure measurements taken during the run.[25]

2. Mean subtraction and SVD truncation for d > 1

For higher values of the delay parameter d, it was found that subtracting the mean from the data did not improve results. This is likely due to the fact that the modified snapshot matrix defined in Eqs. (13) and (14) did not necessarily have a zero temporal mean for each of its rows. In this case, the DMD does not reduce to the DFT which can mean higher reconstruction error despite having potentially physically more relevant modes that capture growth rates. Additionally, and counter-intuitively, a heavier truncation was required to achieve the expected results. This is attributed to the fact that the DMD-1 method suffered a significant loss in reconstruction accuracy even when only a few SVD modes were removed in a truncation (for example, to rank 490 instead of the full 499). If the first truncation for HODMD with $d > 1$ keeps all 499 SVD modes initially, the dimension of the data would be reduced to $500 - d + 1$ upon construction of the modified snapshot matrix in Eq. (14). This is problematic, as the goal of constructing the modified snapshot matrix is to enlarge the dimension of the data.

The amount of SVD truncation that should be performed is not always clear, and this must be chosen carefully. In Ref. 14, the authors mention that large truncations may be required for complex multi-
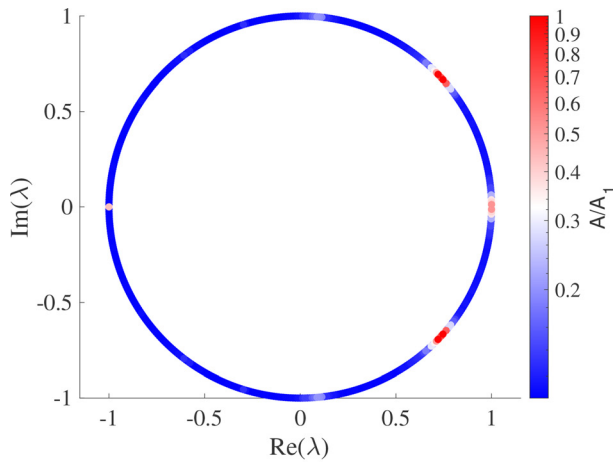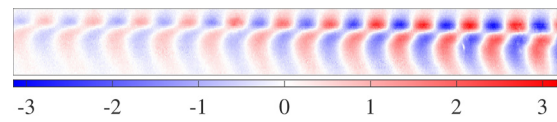
(a) DMD-1 spectrum.
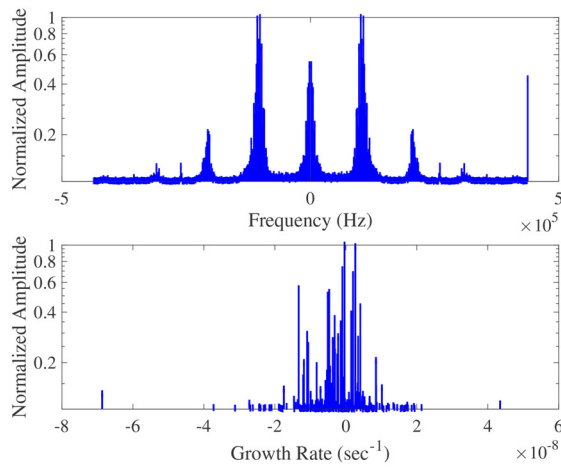
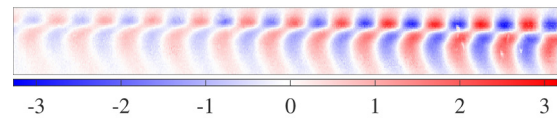(b) DMD-1 frequencies and growth rates.

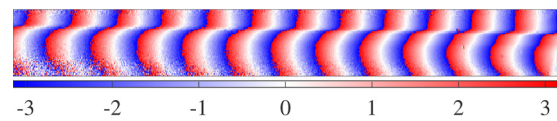**FIG. 5.** DMD-1 frequencies and growth rates for 3-degree cone.

(a) Real component.

(b) Imaginary component.

(c) Magnitude.

(d) Phase.

FIG. 6. DMD-1 106.75 kHz mode contours for 3-degree cone case.

scale (or noisy) data despite the fact that one would otherwise generally want to keep as many SVD modes as possible to capture the full physics embedded in the data. The tolerance ε_{SVD} can be used to compute the lower-rank approximation of the dataset onto which the Koopman matrix R would be projected if $d = 1$. If $d > 1$, the reduced SVD coordinates are those used to compute the modified snapshots and the modified Koopman matrix. Ideally, for simple flows, ε_{SVD} would be set based on the noise level. However, for feature identification in complex or turbulent flows, the tolerance can be relaxed further to remove even smaller scales of turbulent flow in addition to noise.[14,26] Alternatively, the truncation value can be set directly by keeping only the leading SVD modes. This truncation can reduce the accuracy of standard DMD. This is because the dimension-reduced snapshots may still contain a very high spectral complexity.

DMD with a truncated SVD computes the best-fit linear operator that advances the time coefficients of the leading SVD modes one time step into the future. Because the SVD is dimension-reduced, the

higher-order Koopman assumption can be more accurate than the standard DMD approximation and augment the spatial dimension. In this way, the HODMD method allows one to analyze the time dynamics of the most energetic SVD modes in a way that standard DMD can fail to do due to the low rank of the dimension-reduced data. This also partially elucidates the reason that HODMD works better with a heavier truncation than standard DMD—the kept higher energy SVD modes can contain a great deal of spectral complexity that requires augmentation beyond the $K - d + 1$ limit in Eq. (13). Truncating the SVD then, which reduces the spatial complexity, will also limit the spectral complexity that could be captured by the standard DMD. With HODMD, the full spectral complexity of the truncated data can be found as long as it is less than $K - d + 1$. Standard DMD without dimension reduction can result in noisy modes and could even lead to spurious results. Dimension reduction can help clean the noise as long as the spectral complexity of the remaining SVD modes is not much higher than the number of retained modes. Of course, as stated above, DMD can reduce to a DFT in which case the data will be represented almost exactly with $RRMSE \ll 1$, though this may not be desirable depending on the exact scenario.

These factors motivate using a larger tolerance for the initial SVD truncation. As shown above, the DMD-1 with no truncation identified expected peak frequencies and mode shapes, but the modes were still noisy—the small RRMSE means the noise was reconstructed too. In addition, the DMD-1 method produced many low-amplitude modes that contained only (or mostly) noise. On the one hand, the small-amplitude modes could be removed after the computation of the DMD expansion. However, the DMD-1 modes found above still contain background noise. Thus, although leaving in the noise for DMD-1
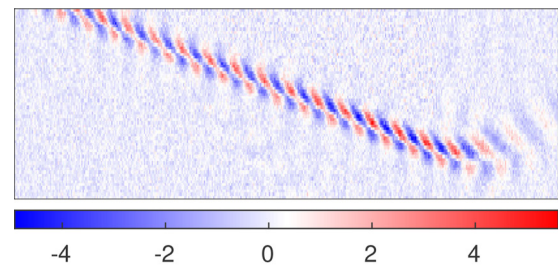
18 September 2024 14:25:30
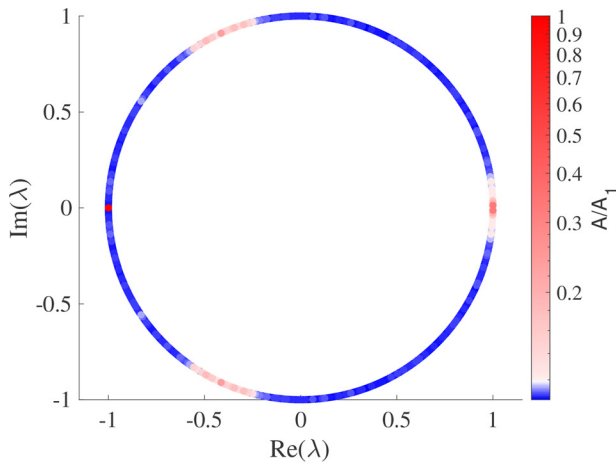
(a) DMD-1 spectrum.
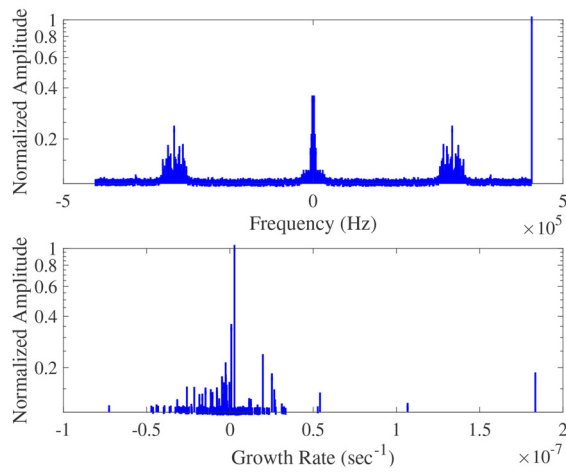
(b) DMD-1 frequencies and growth rates.

FIG. 7. DMD-1 frequencies and growth rates for 7-degree cone.

(a) Real component.

(b) Imaginary component.

(c) Magnitude.

(d) Phase.

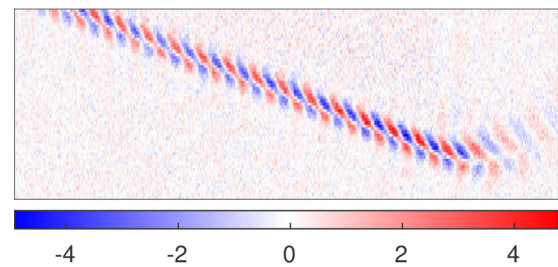**FIG. 8.** DMD-1 278.25 kHz mode contours for 7-degree cone case.

produced accurate results in terms of the data reconstruction, it was desirable to apply the HODMD with $d > 1$ as well. Thus, it was seen as desirable to remove noise via a truncated HOSVD and apply DMD-d and DMD-1. The subsequent sections detail noise estimation, application of DMD-d with $d > 1$ with HOSVD, and DMD-1 with HOSVD before the final spatiotemporal analysis with STKD.

3. Estimation of noise from DMD-1

The amplitude vs frequency plot in Fig. 5(b) was used to truncate the DMD expansion to filter noise. The kept modes are marked on the frequency plot (Fig. 9) below with a circle. In addition to removing the small-amplitude modes via setting $\varepsilon_{amp} = 1.2 \times 10^{-1}$, the high-amplitude mode with a frequency of 437.5 kHz was removed. This is because a visual inspection of the mode shows only incoherent noise. Figure 10 shows the 400th snapshot of the original data and cleaned (reconstructed) data. The cleaned dataset retained 106 modes,
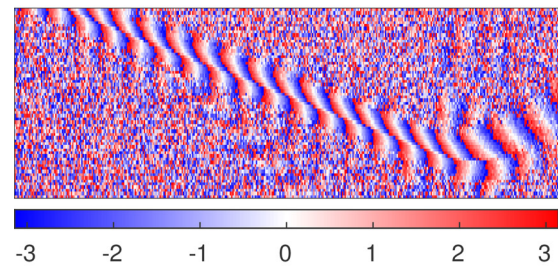
meaning the rank of the reconstruction was 106. Interestingly, the reconstruction error for keeping these higher-amplitude modes reaches $RRMSE \approx 5.56 \times 10^{-1}$. This implies that the noise makes up a significant portion of the fluctuating component of the pixel value. This highlights the key difference that must be noted when setting ε_{SVD} with Eqs. (6) vs (8). This allows a set tolerance based on a known noise level or a desired reconstruction error based on the Frobenius norm. Ultimately, the $\varepsilon_{HOSVD} = 1.2 \times 10^{-1}$ tolerance was used in the

DMD-1 with HOSVD analysis below for the spatial HOSVD mode matrices to remove background noise. A similar analysis was done to determine the noise levels for the 7-degree cone.

The singular values from the SVD of the snapshot matrix are given in Fig. 11. The comparison to the ε_{SVD} is shown as well. This criterion indicates that the dimension of the data should be limited to approximately $r = 27$. It is seen in the figure that the singular values level off relatively soon after this value. The standard DMD (DMD-1) gives spurious time dynamics with this large of a truncation. This is the general motivation for using DMD-d with $d > 1$. However, good time dynamics (low RRMSE of the reconstruction) were found with a delay parameter of $d = 1$ for the mean-subtracted dataset. For that reason, the truncated HOSVD was applied to add spatial filtering without heavily reducing the spatial complexity for the temporal analysis (truncating the rank of X and Y but no T truncation). The results of this analysis are presented in Sec. VI A 4.

4. DMD-1 with truncated HOSVD

Due to good but noisy results from DMD-1 without truncation, DMD-1 with truncated HOSVD was done. The tolerance ε_{SVD} was set at the noise level in Sec. VI A 3, 1.2×10^{-1} for the spatial dimensions, while the temporal tolerance was set much lower (1.0×10^{-4}) such that no temporal modes were removed. This meant the number of modes in each direction were $(P_1, P_2, P_3) = (49, 13, 499)$. This resulted in very similar results to the DMD-1 without truncation, but much of the noise was removed. One small difference is that the final amplitudes of each mode were slightly different because the spatial mode shapes reconstructed from the reduced HOSVD mode matrices were rescaled to have unit RMS norm. The singular values from the HOSVD are given in Fig. 12. The results for the mode shape of the 106.75 kHz mode are given in Fig. 13.

The HOSVD singular values for the different dimensions of the 7-degree cone snapshot tensor are given in Fig. 14. For a similar analysis to the 3-degree case, and to promote filtering in the directions tangent and normal to the cone surface, the video of the 7-degree cone was rotated 7 degrees and further cropped. Thus, the x and y directions remain consistent for filtering. The results for the mode shapes of the 7-degree cone are given in Fig. 15. Note that these are displayed now with x and y defined above being the horizontal and vertical directions rather than the original orientation shown in Fig. 8. For this case, the HOSVD spatial ε tolerance was set to 1.5×10^{-1}, which kept mode numbers $(P_1, P_2, P_3) = (151, 14, 500)$. The original sizes were
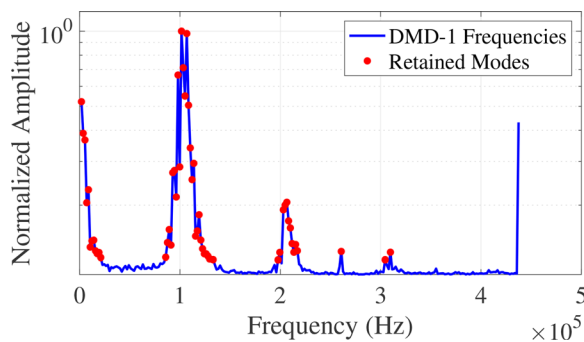

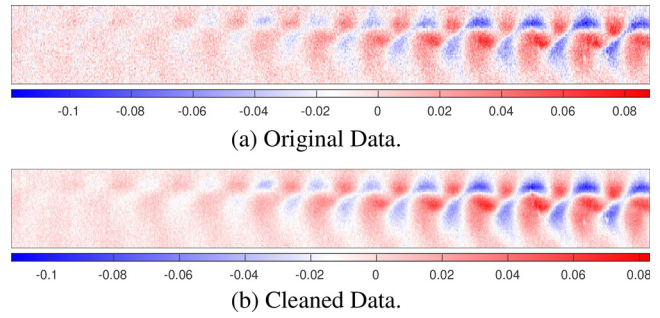(a) Original Data.

(b) Cleaned Data.

FIG. 10. Original vs cleaned mean-subtracted data for 3-degree cone. The 400th time step reconstruction is shown here.
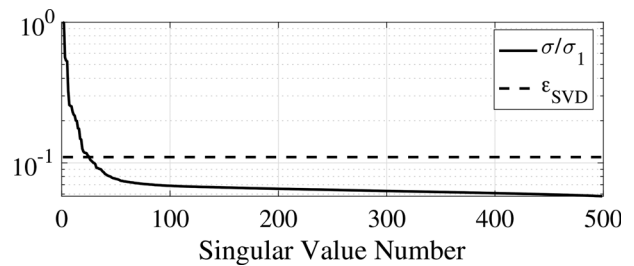

FIG. 11. Singular values (σ_n/σ_1) for mean-subtracted 3-degree cone video.

$(I, J, K) = (360, 14, 500)$. Although the spatial resolution is somewhat low, the mode shapes capture the wavepacket structure along with intensity amplification from the magnitude plot despite the low spatial resolution.

5. DMD-150

For the 3-degree cone, DMD-150 was chosen based on the consistency of results and reconstruction error. The initial truncation was performed by setting $\varepsilon_{SVD,1} = \varepsilon_{SVD,2} = 1.2 \times 10^{-1}$, just below the noise level described in the previous section. This was implemented with Eq. (8). Figure 11 shows the singular values normalized by the maximum singular value for the initial SVD. It is clear that this is a high tolerance, and only 27 modes result from this. The low frequencies are present as well as the cluster around 106 kHz. Based on the idea presented in Ref. 27 for finding the most important dynamics that could be embedded in noisy experimental data, we applied the iterative
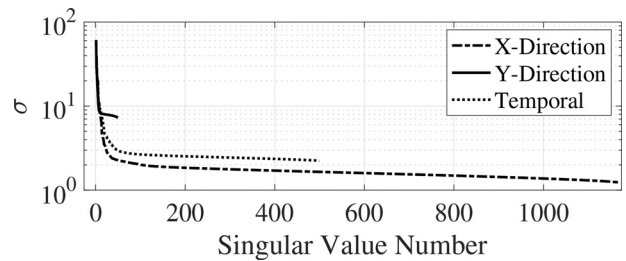

FIG. 9. Retained modes for noise filtering for 3-degree cone.

FIG. 12. HOSVD singular values for temporal mean-subtracted 3-degree cone video.

(a) Real component.

(b) Imaginary component.

(c) Magnitude.

(d) Phase.
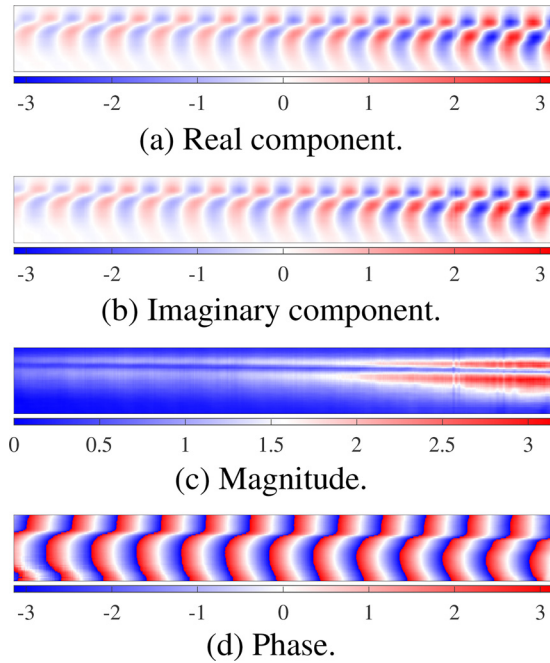
FIG. 13. DMD-1 with HOSVD 106.75 kHz mode contours for 3-degree cone case.

(a) Real component.

(b) Imaginary component.

(c) Magnitude.

(d) Phase.

FIG. 15. DMD-1 with HOSVD 278.25 kHz mode contours for 7-degree cone case. Flow is moving left to right, and the surface normal direction is vertical.

version of DMD-150. This meant applying the algorithm, reconstructing, and re-applying the algorithm to the reconstruction until the number of retained modes from the same tolerances remained constant. Spurious artifacts can be removed along the way during the reconstruction stages. For this analysis, a tighter tolerance of $\varepsilon_{HOSVD} = \varepsilon_{SVD,2} = 6.54 \times 10^{-2}$ was used. This was chosen to retain the first 200 SVD modes. The second SVD (on the modified snapshots) reduced the dimension to 107. However, the benefits of this iteration were not clear because the results did not significantly improve before desired modes like the higher harmonics of the primary second mode disturbance frequency in the 3-degree cone video started to be removed. Truncating too much resulted in eigenvalues with damping rates that were potentially unphysical. This is improved by increasing the delay parameter. However, as mentioned earlier, the delay parameter cannot be too large compared to the number of snapshots so this did not alleviate the high damping rates. Thus, for the temporal analysis, mean subtraction with a delay parameter of one and no truncation was considered sufficient. Essentially, we exploited the reduction of
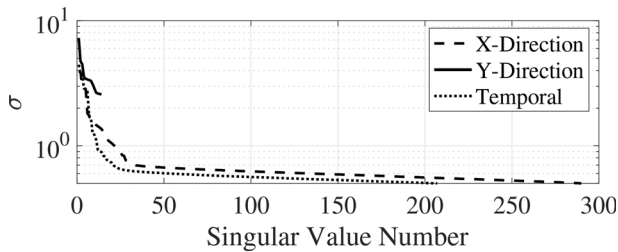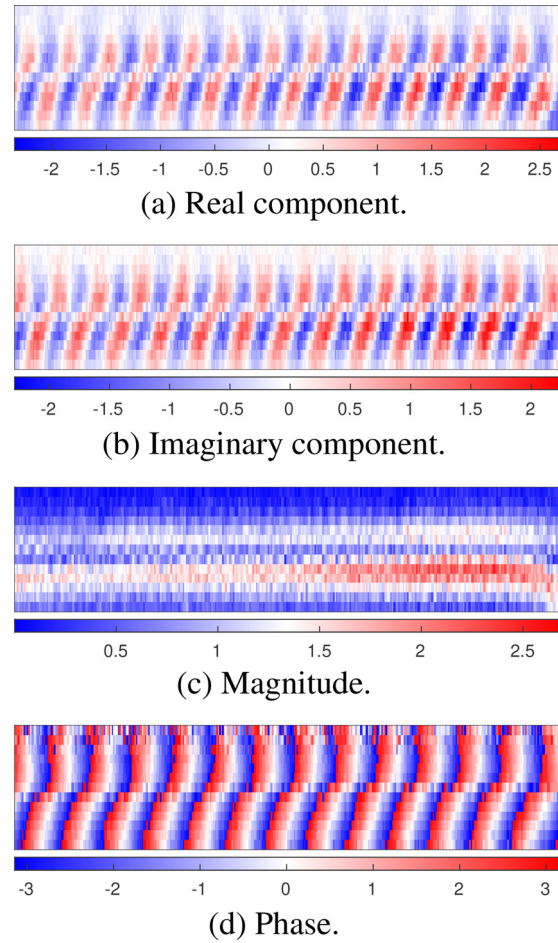
DMD-1 to a DFT to obtain purely oscillatory time dynamics and reserved the DMD-d algorithm for the spatial analysis. As will be discussed, obtaining physically meaningful spatial growth required the higher-order algorithm.

B. Spatiotemporal analysis: STKD

The STKD algorithm was implemented to the videos organized as snapshot tensors. The input data were exactly that used in Sec. VI A 4. The output of the STKD is a set of modes that are a function of the surface normal coordinate y. These modes are associated with growth rates and wavenumbers in the surface-tangent direction and in time. The mode shapes, dispersion diagrams, and growth rates for both cases are given below. For scatter plots in this section, the color bar represents normalized amplitude a_{mn} of the STKD modes, which differ from the amplitudes for the temporal (a_n^t) and spatial analyses (a_m^x), unless otherwise noted in the figure description.

For the 3-degree cone case, the application of the HOSVD gave the singular values shown in Fig. 12. The same values of P_1, P_2, and P_3 were used as before. The delay parameter for DMD-d of the spatial

FIG. 14. HOSVD singular values for temporal mean-subtracted 7-degree cone video.

18 September 2024 14:25:30

matrix was 300, while DMD-1 was used for the temporal matrix. This is because DMD-1, as shown above, gave frequencies that aligned with experimental measurements. However, although DMD-1 was able to reconstruct the X HOSVD mode matrix with a small error, the spatial modes computed were spurious and did not capture the spatial growth clearly present in the mode shapes from DMD-1. This is related to the DMD–DFT equivalence, where exponential growth is implicitly given by the wavenumber spectrum rather than explicitly represented through growth rates. Thus, DMD without mean subtraction and with a higher delay parameter than 1 was chosen for the spatial analysis. DMD-300 allowed for the physically expected modes (modes with non-zero growth rates associated with frequencies whose DMD-1 mode shapes show clear growth) to be computed, as will be shown below.

The dispersion diagram from the analysis along with spatial growth rates is shown in Fig. 16. The traveling waves representing the fluctuating components of the video are clear, due to the general trend of the negative slope in the dispersion diagram. This is because wave speed c is given by the relation $c = -\omega/\kappa$. Thus, there are a number of traveling waves with wave speed given by the slope of the line connecting each point in Fig. 16(a) to the origin.

For the 7-degree cone case, the same values of P_1, P_2, and P_3 were used as the DMD-1 with HOSVD case. A delay parameter of 60 was found to be the most effective. This is smaller than that used for the 3-degree cone case. This is because the delay parameter scales with the number of snapshots, which for the spatial analysis corresponds to $I = 360$ for the 7-degree case. The 7-degree cone case counterpart of Fig. 16 is given in Fig. 17. Figure 17(b) shows the various growth rates colored by normalized spatial amplitudes a_m^x. It is noted that truncation based on amplitudes via Eq. (30) here needed to be done carefully, as a significant flow feature could have a small amplitude but a high growth rate to best fit the data. Then, the high growth rate would result in the importance of the mode shape relative to other higher-amplitude modes. The figure shows the most relevant STKD modes are waves traveling between 700 and 900 m/s that have positive spatial growth rates.

Another way the STKD can be beneficial is by plotting the mode shapes just as was done for the purely temporal analysis. This shows the variation in disturbance magnitude with surface normal coordinates. Here, only two representative high-amplitude modes are plotted, though there are $M \times N$ STKD modes before truncation based on amplitudes. For the 7-degree cone, a representative mode $u_{1,2}$ was plotted since it is the mode associated with the highest amplitude frequency (278.25 kHz) and highest spatial growth rate. The absolute value of the complex mode shape is plotted in Fig. 18. For the 3-degree cone case, the highest amplitude mode $u_{2,1}$ is plotted in Fig. 19. The 3-degree mode shape visually appears more jagged despite the higher spatial resolution, but the variation in the y-direction corresponds with the visual variation in the absolute value of the spatial mode shapes [for example, in Fig. 13(c)].

VII. N-FACTORS FROM HODMD AND STKD

The N-factor is the natural log of the ratio of a disturbance's amplitude at one point in space to its initial location. The N-factor can be calculated as the integrated growth rate along the x-direction. For DMD, the value

$$\Delta N_{\mathrm{DMD}}(x_i, y_j) = \ln\left[A(x_i, y_j)/A_1\right], \tag{32}$$

was taken, where $A_1 = A(x_1, y_j)$ and A was defined in Eq. (31). This formula corresponds with the formulation used for examining cross-flow instabilities by Le Clainche et al.[8] The DMD N-factor is then a function of the surface normal coordinate and can vary nonlinearly with the streamwise direction. In Fig. 20, we present an estimate of the change in N-factor ΔN for the 3-degree cone mode at 101.5 kHz is plotted along the change in streamwise coordinate Δx. The trend follows expected shapes from LST calculations.[23] For this plot, the value at $y_{j=38} = 2.8$ mm is given as a representative example.

For STKD, the growth rates are fixed for a given frequency and sample domain, which allows an estimation of N-factor from

$$\Delta N_{\mathrm{STKD}}(x_i) = \nu_{\max}(x_i - x_0). \tag{33}$$

The STKD N-factor defined in Eq. (33) is useful for estimating transition location as it shows the maximum exponential growth in the domain of the data and therefore the most dominant growing wave. For this reason, this formula was used to estimate transition by estimating the maximum growth of T–S waves in previous studies
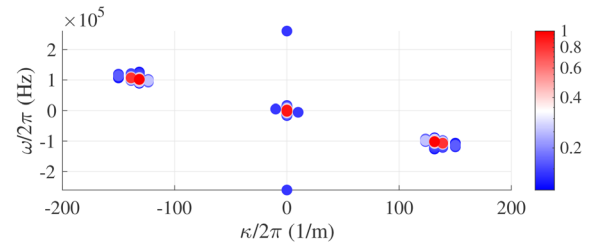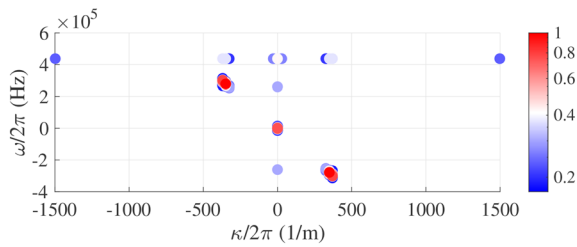

(a) Dispersion diagram.
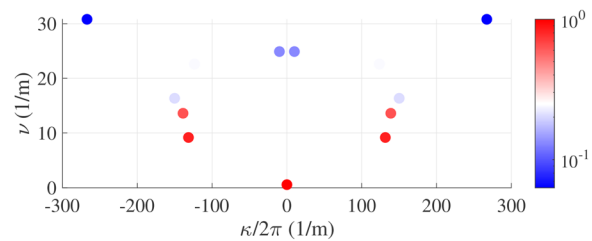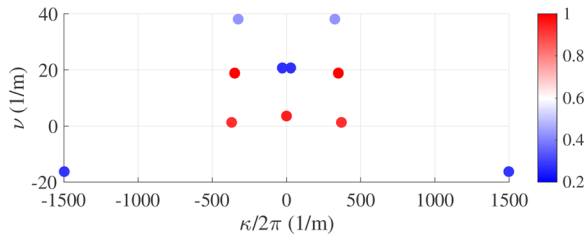

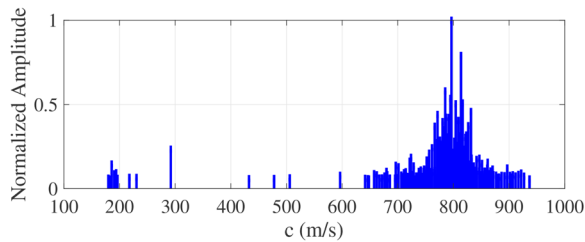(b) Spatial growth rates colored by normalized a_m^x.
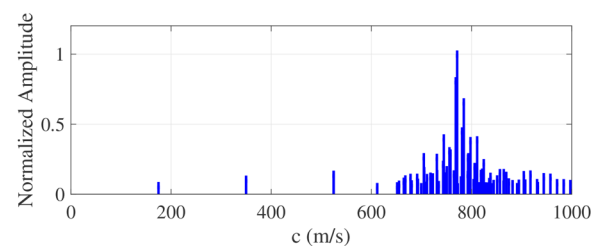
(c) Wavespeed.

FIG. 16. STKD dispersion diagram, growth rates, and wave speed for 3-degree cone case.

(a) Dispersion diagram.

(b) Spatial growth rates colored by normalized a_m^x.

(c) Wavespeed.

FIG. 17. STKD dispersion diagram, growth rates, and wave speed for 7-degree cone case.

with the purely spatial analysis.[7] A similar plot to Fig. 20 could be made from STKD results, but this would only give straight lines based on Eq. (33). Alternatively, the STKD could be used to reconstruct (approximately) the corresponding HODMD mode for a given frequency ω_n by summing over all m in Eq. (4). This way, the additional spatial filtering inherent to the STKD will make the result smoother. However, the STKD results allow a more efficient way to visualize the
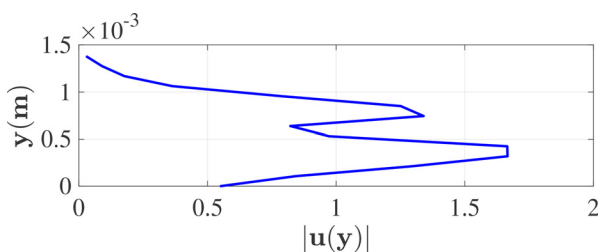

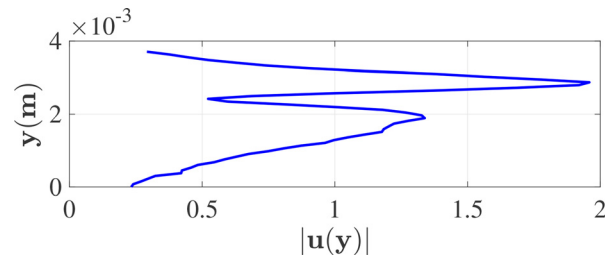**FIG. 18.** Plot of mode shape $|u_{1,2}(y)|$ for 7-degree cone case.

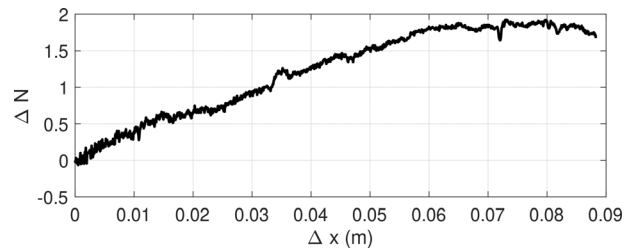**FIG. 19.** Plot of mode shape $|u_{2,1}(y)|$ for 3-degree cone case.

FIG. 20. DMD estimate of ΔN for 101.5 kHz mode.

approximated maximum growth: a scatterplot of the growth rates for each frequency colored by amplitude. These plots are given in Figs. 21 and 22 for the 7° and 3° cases, respectively. These plots are useful because, based on Eq. (33), the y-axis represents the change in N-factor per unit change in x. Therefore, for example, a red dot means a high-amplitude mode, the y-location of that dot gives the value of $\Delta N_{STKD}/\Delta x$, and the x-axis gives the associated frequency.

VIII. CONCLUSION

The spatiotemporal Koopman decomposition developed by Le Clainche and Vega was applied to Mach 6 flow schlieren videos depicting second mode instability waves. Crucial parameters such as wave speeds, temporal frequencies, growth rates, and spatial wavenumbers were computed. The standard DMD–DFT similarity for mean-subtracted data was exploited to decompose the data into spatially growing waves with fixed wave speeds and time dynamics without growth or decay. Additionally, spatial mode shapes obtained through temporal analysis involving DMD-1 with HOSVD elucidated wave-packet structures and spatial growth. Compared to conventional methods, the application of STKD yielded clearer results due to the superior spatial filtering capabilities and explicit modeling of coupled
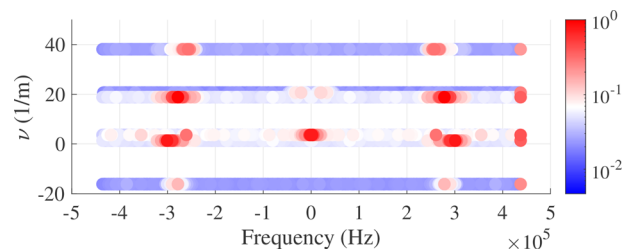

FIG. 21. Spatial growth rates vs temporal frequencies for 7-degree cone.
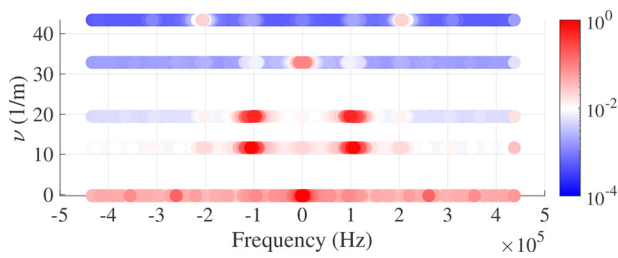
FIG. 22. Spatial growth rates vs temporal frequencies for 3-degree cone.

spatiotemporal dynamics. The ability to determine wave speeds and spatial growth rates is clearly advantageous for tracking disturbances in unsteady experimental or numerical datasets. This study has presented the power of advanced spatiotemporal decomposition techniques in unraveling complex flow phenomena from schlieren video data via application to videos that clearly depicted the desired physics. Future work remains in improving results for tracking single frequency single wavenumber disturbance growth from various data sources that depict many more flow features in addition to noise, where the filtering process with the HOSVD and amplitude truncations could be more difficult. Despite potential difficulties with truncation tolerances, the ability of the STKD with HODMD and HOSVD to perform well for multiscale noisy data suggests that the method could be more readily applied to flows where traditional methods like LST and PSE fail, for example, beyond the laminar regime. Eventually, applying Le Clainche and Vega's STKD algorithm to more complex unsteady experimental datasets like schlieren videography, including videos that potentially do not depict the desired flow structures as clearly as those in the present study, should be able to provide fast low-cost estimates of wavespeeds, magnitude, and growth rates of various flow structures in addition to modal growth.

ACKNOWLEDGMENTS

AUTHOR DECLARATIONS
Conflict of Interest

The authors have no conflicts to disclose.

Author Contributions

Arman C. Ghannadian: Data curation (equal); Formal analysis (equal); Investigation (equal); Methodology (equal); Software (equal); Validation (equal); Visualization (equal); Writing – original draft (equal). **Ryan C. Gosse:** Conceptualization (equal); Funding acquisition (equal); Investigation (equal); Project administration (equal); Resources (equal); Writing – review & editing (equal). **Subrata Roy:** Conceptualization (equal); Funding acquisition (equal); Investigation (equal); Methodology (equal); Project administration (equal); Resources (equal); Supervision (lead); Writing – review & editing (equal). **Zachary D. Lawless:** Data curation (equal); Visualization (equal); Writing – original draft (equal). **Samantha A. Miller:** Data curation (equal); Investigation (equal). **Joseph S. Jewell:** Funding acquisition (equal); Project administration (equal); Resources (equal); Supervision (equal); Writing – review & editing (equal).

DATA AVAILABILITY

The data that support the findings of this study are available from the corresponding author upon reasonable request.

REFERENCES

[1]L. M. Mack, "Boundary-layer linear stability theory: Special course on stability and transition of laminar flow," AGARD Report No. 709 (Advisory Group for Aerospace Research and Development, NATO, 1984).

[2]T. Herbert, "Parabolized stability equations," Annu. Rev. Fluid Mech. **29**, 245–283 (1997).

[3]S. Le Clainche and J. M. Vega, "Spatio-temporal Koopman decomposition," J. Nonlinear Sci. **28**, 1793–1842 (2018).

[4]P. J. Schmid, "Dynamic mode decomposition and its variants," Annu. Rev. Fluid Mech. **54**, 225–254 (2022).

[5]S. Le Clainche and J. M. Vega, "Higher order dynamic mode decomposition," SIAM J. Appl. Dyn. Syst. **16**, 882–925 (2017).

[6]M.-M. Wu, Z.-H. Han, S.-N. Wang, W.-P. Song, and E. Ferrer, "A DMD-based automatic transition prediction method for flows over airfoils," AIAA Paper No. AIAA 2017-4303, 2017.

[7]M. Wu, Z. Han, H. Nie, W. Song, S. L. Clainche, and E. Ferrer, "A transition prediction method for flow over airfoils based on high-order dynamic mode decomposition," Chin. J. Aeronaut. **32**, 2408–2421 (2019).

[8]S. Le Clainche, Z.-H. Han, and E. Ferrer, "An alternative method to study cross-flow instabilities based on high order dynamic mode decomposition," Phys. Fluids **31**, 094101 (2019).

[9]B. Chen, M. C. Ekwonu, and H. Samsam-Khayani, "Robust modal decomposition of low-resolution schlieren visualization of supersonic flows," J. Visualization **25**, 923–928 (2022).

[10]J. Weiss, "A tutorial on the proper orthogonal decomposition," AIAA Paper No. AIAA 2019-3333, 2019.

[11]K. Taira, S. L. Brunton, S. T. M. Dawson, C. W. Rowley, T. Colonius, B. J. McKeon, O. T. Schmidt, S. Gordeyev, V. Theofilis, and L. S. Ukeiley, "Modal analysis of fluid flows: An overview," AIAA J. **55**, 4013–4041 (2017).

[12]J. H. Tu, C. W. Rowley, D. M. Luchtenburg, S. L. Brunton, and J. N. Kutz, "On dynamic mode decomposition: Theory and applications," arXiv:1312.0041 (2013).

[13]A. Towne, O. T. Schmidt, and T. Colonius, "Spectral proper orthogonal decomposition and its relationship to dynamic mode decomposition and resolvent analysis," J. Fluid Mech. **847**, 821–867 (2018).

[14]B. Begiashvili, N. Groun, J. Garicano-Mena, S. Le Clainche, and E. Valero, "Data-driven modal decomposition methods as feature detection techniques for flow problems: A critical assessment," Phys. Fluids **35**, 041301 (2023).

[15]A. Martínez-Sánchez, E. Lazpita, A. Corrochano, S. Le Clainche, S. Hoyas, and R. Vinuesa, "Data-driven assessment of arch vortices in simplified urban flows," Int. J. Heat Fluid Flow **100**, 109101 (2023).

[16]S. Le Clainche, X. Mao, and J. Véga, "Spatio-temporal Koopman Decomposition in offshore wind turbines," in 17th International Symposium on Transport Phenomena and Dynamics of Rotating Machinery (ISROMAC2017), Maui, 2017.

[17]S. Le Clainche, J. M. Pérez, J. M. Vega, and J. Soria, "Near and far field laminar flow structures in an axisymmetric zero-net-mass-flux jet," Aerosp. Sci. Technol. **105**, 105920 (2020).

[18]J. M. Pérez, S. Le Clainche, and J. M. Vega, "Reconstruction of three-dimensional flow fields from two-dimensional data," J. Comput. Phys. **407**, 109239 (2020).

[19]B. C. Chynoweth, J. B. Edelman, K. A. Gray, G. R. McKiernan, and S. P. Schneider, "Measurements in the Boeing/AFOSR Mach-6 quiet tunnel on hypersonic boundary-layer transition," AIAA Paper No. AIAA 2017-3632, 2017.

[20]B. C. Chynoweth, "Measurements of transition dominated by the second-mode instability at Mach 6," Ph.D. thesis (Purdue University, 2018).

[21]D. V. Mamrol and J. S. Jewell, "Freestream noise in the Purdue University Boeing/AFOSR Mach-6 quiet tunnel," AIAA Paper No. AIAA 2022-2453, 2022.

[22]S. M. Hirsh, K. D. Harris, J. N. Kutz, and B. W. Brunton, "Centering data improves the dynamic mode decomposition," SIAM J. Appl. Dyn. Syst. **19**, 1920–1955 (2020).

[23]S. A. Miller, J. J. Redmond, K. Jantze, C. Scalo, and J. S. Jewell, "Investigation of second-mode instability attenuation over porous materials in Mach-6 quiet flow," in *AIAA Aviation 2022 Forum* (AIAA, 2022).

[24]K. K. Chen, J. H. Tu, and C. W. Rowley, "Variants of dynamic mode decomposition: Boundary condition, Koopman, and Fourier analyses," J. Nonlinear Sci. **22**, 887–915 (2012).

[25]Z. Lawless, E. Nicotra, and J. S. Jewell, "Base flow measurements of a slender cone at Mach 6," AIAA Paper No. AIAA 2024-2329, 2024.

[26]S. Le Clainche and J. M. Vega, "Higher order dynamic mode decomposition to identify and extrapolate flow patterns," Phys. Fluids **29**, 084102 (2017).

[27]S. Le Clainche, J. M. Vega, and J. Soria, "Higher order dynamic mode decomposition of noisy experimental data: The flow structure of a zero-net-mass-flux jet," Exp. Therm. Fluid Sci. **88**, 336–353 (2017).

[28]N. Groun, M. Villalba-Orero, E. Lara-Pezzi, E. Valero, J. Garicano-Mena, and S. Le Clainche, "Higher order dynamic mode decomposition: From fluid dynamics to heart disease analysis," Comput. Biol. Med. **144**, 105384 (2022).

[29]J. H. Tu, "Dynamic mode decomposition: Theory and applications," Ph.D. dissertation (Princeton University, 2013).

18 September 2024 14:25:30